Total reaction cross sections from ^{141}Pr(α,α)^{141}Pr elastic scattering and α-induced reaction cross sections at low energies

Peter Mohr[1,2,*]

[1]*Diakonie-Klinikum, D-74523 Schwäbisch Hall, Germany*
[2]*Institute of Nuclear Research (ATOMKI), H-4001 Debrecen, Hungary*
(Received 5 August 2011; revised manuscript received 6 October 2011; published 15 November 2011)

Elastic scattering data for ^{141}Pr(α,α)^{141}Pr have been analyzed to derive a new energy-dependent local potential for the ^{141}Pr-α system. This potential is used successfully to predict the cross section of the ^{141}Pr(α,n)^{144}Pm reaction at low energies where new experimental data have become available very recently. In contrast to various global potentials, this new potential is able to reproduce simultaneously elastic scattering data around and above the Coulomb barrier and reaction data below the Coulomb barrier for the ^{141}Pr-α system. Reasons for the partial failure of the global potentials are explained by intrinsic properties of the scattering matrix and their variation with energy. The new local potential may become the basis for the construction of a new global α-nucleus potential.

I. INTRODUCTION

The total reaction cross section $\sigma_{\rm reac}$ is related to the complex scattering matrix $S_L = \eta_L \exp{(2i\delta_L)}$ by the well-known relation

$$\sigma_{\rm reac} = \sum_L \sigma_L = \frac{\pi}{k^2} \sum_L (2L+1)\left(1 - \eta_L^2\right), \qquad (1)$$

where $k = \sqrt{2\mu E_{\rm c.m.}}/\hbar$ is the wave number, $E_{\rm c.m.}$ is the energy in the center-of-mass (c.m.) system, and η_L and δ_L are the real reflection coefficients and scattering phase shifts. σ_L is the contribution of the Lth partial wave to the total reaction cross section $\sigma_{\rm reac}$.

Usually, experimental elastic scattering angular distributions are analyzed using a complex optical potential. At first view, it seems to be a simple task first to determine $\sigma_{\rm reac}$ from the analysis of the elastic scattering angular distribution and second to distribute this cross section $\sigma_{\rm reac}$ among the open channels (e.g., using the statistical model) to predict cross sections of α-induced reactions. However, in practice several problems appear. There is no unambiguous way to determine reflection coeffcients η_L, phase shifts δ_L, or the optical potential from a measured elastic scattering angular distribution, and, in addition, in most cases angular distributions are measured at relatively high energies whereas reaction cross sections should also be known at low energies below the Coulomb barrier (which holds in particular for reaction cross sections relevant for nuclear astrophysics). Thus, typically an ambiguous optical potential has to be extrapolated down to low energies; as a consequence, considerable uncertainties have been noticed for the prediction of α-induced reaction cross sections at low energies, in particular for (α,γ) capture reactions for targets with masses above $A \approx 100$ [1–7].

Very recently, Sauerwein *et al.* [8] have studied the ^{141}Pr(α,n)^{144}Pm reaction at energies between 10 and 15 MeV, i.e., below the Coulomb barrier. It is shown in [8] that the calculated ^{141}Pr(α,n)^{144}Pm cross section depends almost

exclusively on the α transmission and is thus well suited to test global α-nucleus optical potentials. It is found that the new experimental data cannot be reproduced by any of the widely used global α-nucleus potentials, which are the energy-independent four-parameter McFadden-Satchler (MCF) potential [9], the latest version of the Avrigeanu (AVR) potential with many partly energy-dependent parameters [10], and the energy-independent six-parameter potential by Fröhlich and Rauscher (FRR), which is optimized for low-energy reaction cross sections [11]. However, an excellent description of the new ^{141}Pr(α,n)^{144}Pm data is achieved in [8] using an energy-dependent modification of the MCF potential where a new energy dependence of the depth of the imaginary Woods-Saxon volume potential was introduced to reproduce the new reaction data; the potential by Sauerwein *et al.* is referred to as Sauerwein-Rauscher (SAR) in the following.

In contrast to the study in [8], which is restricted to the analysis of the ^{141}Pr(α,n)^{144}Pm reaction in a narrow energy window, the present study considers ^{141}Pr(α,α)^{141}Pr elastic scattering in a wide energy range from 19 to 45 MeV. From the fits to the elastic scattering angular distributions a new energy-dependent potential is derived, and the total reaction cross section $\sigma_{\rm reac}$ is calculated from this potential. $\sigma_{\rm reac}$ is then compared to all available α-induced reaction data on ^{141}Pr in the EXFOR data base [12]. The aim of the present study is thus to obtain a consistent description of all available elastic scattering and reaction data over a broad energy range.

Elastic ^{141}Pr(α,α)^{141}Pr scattering data are available in the literature at 45 MeV [13]. However, these data cover only a limited angular range, and they have to be digitized from Fig. 3 in [13]. The latter leads to uncertainties which are difficult to estimate. Four ^{141}Pr(α,α)^{141}Pr angular distributions at $E_{\rm lab} = $ 19.0, 23.97, 32.0, and 37.7 MeV have been measured [14]. The experiment has been performed at the XTU Tandem of the INFN Laboratori Nazionali di Legnaro. Unfortunately, these data have never been published; a partial analysis of the data was already shown in an earlier publication [15]. These data are available in numerical form (including uncertainties) and are thus much better suited for the determination of an optical

───────
*WidmaierMohr@t-online.de

potential by a fitting procedure. However, as the original data give statistical errors only (with tiny uncertainties at forward angles), a 5% uncertainty has been added quadratically to account for unknown systematic errors of the data. Note that it is difficult to achieve much smaller systematic uncertainties for α-scattering experiments (see, e.g., [16,17]). These data will be made available to the community via EXFOR [12].

Besides the ^{141}Pr$(\alpha,n)^{144}$Pm data of [8], the reactions ^{141}Pr$(\alpha,n)^{144}$Pm and ^{141}Pr$(\alpha,2n)^{143}$Pm have been measured in [18] using a stacked-foil activation technique. The data cover an energy range from about 15 to 45 MeV. Although this technique leads to considerable uncertainties at low energies, these data provide further insight into the energy dependence of reaction cross sections and the distribution of the total reaction cross section σ_{reac} among different open channels. Unfortunately, data for ^{141}Pr$(\alpha,\gamma)^{145}$Pm are not available in [12], and because of its lower reaction cross section and unfavorable half-life and decay branches of ^{145}Pm it was not possible to measure the ^{141}Pr$(\alpha,\gamma)^{145}$Pm cross section simultaneously with the ^{141}Pr$(\alpha,n)^{144}$Pm cross section in the recent high-sensitivity activation experiment of [8].

II. ANALYSIS OF ELASTIC SCATTERING AND THE TOTAL REACTION CROSS SECTION σ_{reac}

A. Elastic scattering

The analysis of the ^{141}Pr$(\alpha,\alpha)^{141}$Pr angular distributions follows closely the procedure outlined in earlier work [16,17]. The total potential is composed of the nuclear potential with real and imaginary parts and the real Coulomb potential. The different potentials are discussed in the following.

The real part of the nuclear potential is derived from the folding model; the folding potential is modified by a strength parameter $\lambda \approx 1.2$–1.4 and a width parameter $w \approx 1.0$. (Large deviations from $w \approx 1$ would indicate a failure of the folding model.) To avoid discrete uncertainties from the so-called family problem, real potentials with volume integrals of about $J_R \approx 320$–350 MeV fm^3 have been selected [15]. (Note that the negative signs of volume integrals J_R and J_I are—as usual—omitted in the discussion.)

The imaginary part of the nuclear potential is taken in the usual Woods-Saxon parametrization. It is well known that scattering data at low energies are best described using

an imaginary potential of Woods-Saxon surface type (see, e.g., [19]). This has been confirmed recently in a microscopic calculation of the α-nucleus potential [20]. The same behavior is found in the present study where the angular distributions at $E_{\mathrm{lab}} = 19.0$, 23.97, and 32.0 MeV can be very well reproduced with a pure surface imaginary potential. An additional volume Woods-Saxon potential in the imaginary part does not improve the description of the angular distributions at low energies. However, for an excellent description of the 37.7- and 45.0-MeV data a combination of volume and surface Woods-Saxon potentials for the imaginary part is required; at these energies the volume part is even dominating the imaginary potential.

The Coulomb potential is taken in the usual parametrization of a homogenously charged sphere with a Coulomb radius R_C identical to the root-mean-square (rms) radius of the folding potential without width modification ($w = 1$). This avoids uncertainties from the otherwise somewhat arbitrary choice of the Coulomb radius R_C (often taken as $R_C = 1.2$, 1.3, or 1.4 fm $\times A_T^{1/3}$), which are non-negligible at least at very low energies [21].

The resulting parameters of the potential and the total reaction cross section σ_{reac} are listed in Table I. The fits are compared to the experimental angular distributions in Fig. 1.

In addition to the local potential analysis, a model-independent phase-shift analysis (PSA) has been performed using the technique of [22]. These phase-shift fits show the tendency to relatively high and oscillating cross sections at backward angles where no experimental data are available. Nevertheless, the derived total reaction cross sections σ_{reac} are close to the results of the local potential fit. From the variation of σ_{reac} with the fitting parameters (in particular the maximum fitted angular momentum L_{max}) and from the comparison with the local potential fit, the uncertainty of σ_{reac} can be estimated to be smaller than 3% in all cases except the lowest energy where I estimate an uncertainty of about 7%. This is also consistent with a recent analysis of total reaction cross sections in [31].

As discussed above, the extraction of the total reaction cross section σ_{reac} requires theoretical considerations and is thus somewhat model-dependent. Nevertheless, because of the small sensitivity of σ_{reac} to the chosen model, the total reaction cross section σ_{reac} can be considered as a quasiexperimental quantity. This holds in particular for cases where the elastic scattering angular distributions cover the full

TABLE I. Parameters of the optical potential and the total reaction cross section σ_{reac} derived from ^{141}Pr$(\alpha,\alpha)^{141}$Pr angular distributions.

E_{lab} (MeV)	$E_{\mathrm{c.m.}}$ (MeV)	λ	w	J_R (MeV fm^3)	$r_{R,\mathrm{rms}}$ (fm)	W_V (MeV)	R_V (fm)	a_V (fm)	W_S (MeV)	R_S (fm)	a_S (fm)	J_I (MeV fm^3)	$r_{I,\mathrm{rms}}$ (fm)	χ^2/F	σ_{reac} [a] (mb)	Ref. Exp.
19.0	18.48	1.354	0.994	345.3	5.511		–		17.1	1.358	0.581	45.1	7.451	2.3	465 ± 31	[14]
23.97	23.31	1.270	1.010	338.6	5.604		–		27.5	1.410	0.508	68.2	7.623	0.8	1018 ± 31	[14]
32.0	31.12	1.452	0.958	326.7	5.314		–		36.1	1.290	0.500	73.9	7.012	2.4	1306 ± 39	[14]
37.7	36.66	1.328	0.992	329.3	5.504	-17.8	1.297	0.157	3.9	1.586	0.457	51.7	6.075	5.9	1654 ± 50	[14]
45.0	43.76	1.306	1.012	340.0	5.614	-18.4	1.303	0.107	6.1	1.567	0.436	58.5	6.253	0.4	1874 ± 56	[13]
low energies		1.354	0.994	345.3	5.511		–		Eq. (4)	1.353	0.530	Eq. (4)	7.361	–	–	–
α decay		1.151	1.000[b]	308.8	5.545		–		–	–	–	–	–	–	–	–

[a]From the local potential fit using Eq. (1); uncertainties are estimated from the model-independent phase-shift analysis.
[b]Fixed.
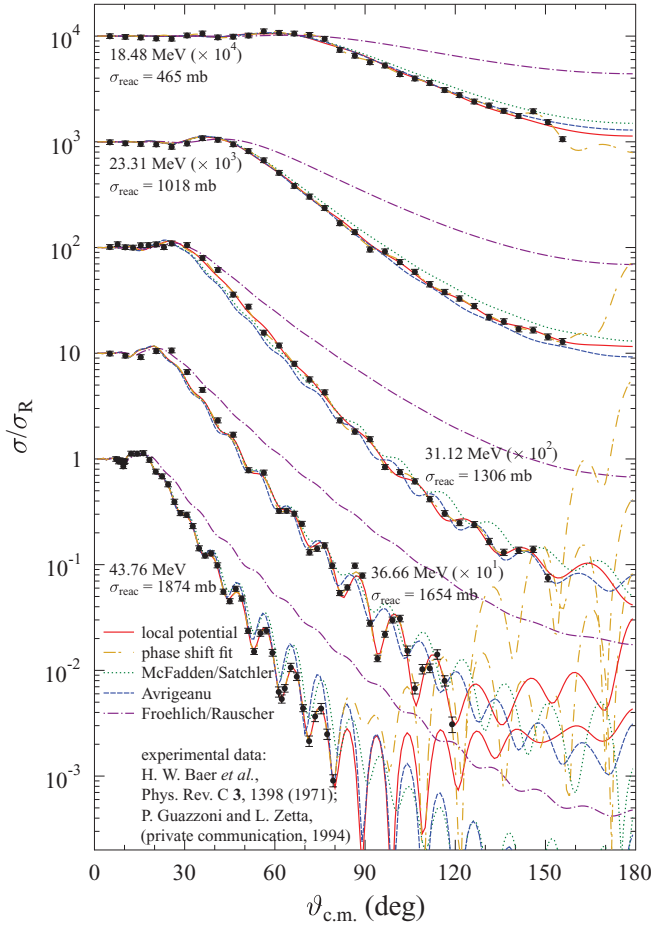
FIG. 1. (Color online) Rutherford normalized elastic scattering cross sections of the ^{141}Pr(α,α)^{141}Pr reaction vs the angle in the center-of-mass frame. The lines are calculated from a local potential fit which is adjusted to the scattering data (full red line), from a phase-shift analysis (dash-dotted light brown line) [22], and from different global α-nucleus potentials [9–11]. The experimental data have been taken from [13,14]. The given energies are $E_{\text{c.m.}}$ in the center-of-mass system.

angular range. However, as a word of caution, it should be kept in mind that discrepancies have been noticed between σ_{reac} determined from elastic scattering angular distributions and from α-transmission experiments [23,24]. These discrepancies have not been fully understood up to now [25].

Furthermore, Fig. 1 shows the results of several global α-nucleus optical potentials [9–11]. It is obvious that the global potentials cannot achieve the same quality as the local potential fit or the phase-shift fit. This is not a surprise because the parameters of the global potentials are not readjusted to the experimental angular distributions. Nevertheless, the AVR potential reproduces the angular distributions very well. The calculations using the MCF potential are also close to the experimental angular distributions; however, there is a systematic overestimation of the scattering cross sections at backward angles at low energies. A strong overestimation at backward angles is found for the FRR potential at all energies; this corresponds to a significant underestimation of the total reaction cross sections σ_{reac} of the FRR potential. It has to be

pointed out here that the FRR potential was never intended to reproduce elastic scattering data above the Coulomb barrier.

The present study does not show results of the potentials of Kumar *et al.* [26] because this potential has been optimized for a wide energy range above the new ^{141}Pr(α,n)^{144}Pm data; in addition, it has been shown in [16] that this potential cannot reproduce ^{89}Y(α,α)^{89}Y elastic scattering data at low energies. Unfortunately, the latest versions [27,28] of the global potential by Demetriou *et al.* [29] are only published in conference proceedings and cannot be used without the authors of [27,28]; I do not intend to show results from the early and perhaps outdated potentials in [29]. Not yet included are also the predictions from a new regional potential which was derived from recent scattering data of the nuclear astrophysics group at Notre Dame University; a publication is in preparation [30].

B. Reduced cross sections

For a comparison of total reaction cross sections for different nuclei at various energies, it has been suggested to present the data as "reduced cross sections" versus "reduced energies" as defined by

$$E_{\text{red}} = \frac{\left(A_P^{1/3} + A_T^{1/3}\right) E_{\text{c.m.}}}{Z_P Z_T}, \tag{2}$$

$$\sigma_{\text{red}} = \frac{\sigma_{\text{reac}}}{\left(A_P^{1/3} + A_T^{1/3}\right)^2}. \tag{3}$$

The reduced energy E_{red} takes into account the different heights of the Coulomb barrier in the systems under consideration, whereas the reduced reaction cross section σ_{red} scales the measured total reaction cross section σ_{reac} according to the geometrical size of the projectile-plus-target system. A smooth behavior for all σ_{red} of α-induced reactions is found, including the new data for ^{141}Pr-α. The obtained values for σ_{red} are smaller for tightly bound projectiles (α, ^{16}O) compared to weakly bound projectiles (^{6,7,8}Li) and halo projectiles (^{6}He). The data are shown in Fig. 2, which is an update of similar figures in [31,32]. Up to now, no complete theoretical analysis has been presented for the reduced cross sections σ_{red} in Fig. 2, and for better readability the data points have been connected by lines to guide the eye (dotted lines in Fig. 2; taken from [32]). In addition to these lines, I show here the result from the local potential for ^{141}Pr(α,α)^{141}Pr with its energy dependence as discussed in Sec. II C. This calculation reproduces practically all data points for α-induced reactions and also data for ^{16}O-^{138}Ba, which is another combination of doubly-magic projectile and semimagic target nucleus.

The smooth behavior of all reduced cross sections σ_{red} in Fig. 2 encourages us to search for a global potential which is able to reproduce σ_{red} and thus the energy dependence of the total reaction cross sections σ_{reac} for α-induced reactions. The present study was restricted to ^{141}Pr but an extension to a wider target range is planned for the near future. The following procedure is applied to derive an energy-dependent α-^{141}Pr potential from the local potential fits (see also Table I).

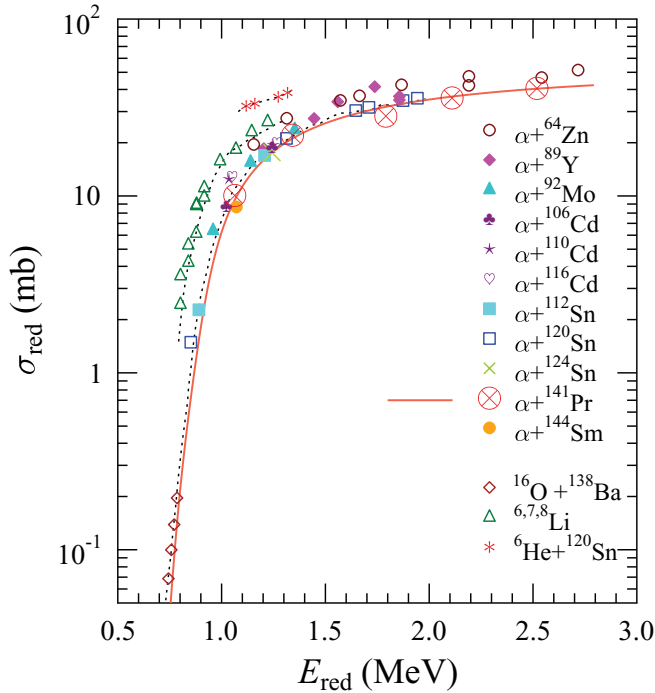FIG. 2. (Color online) Reduced reaction cross sections $\sigma_{\rm red}$ vs reduced energy $E_{\rm red}$ for tightly bound α particles and ^{16}O, weakly bound ^{6,7,8}Li projectiles, and exotic ^{6}He (updated from Fig. 4 of [32] with additional data from [16,17,31,33,34]). The error bars of the new data for ^{141}Pr (huge red symbols) are omitted because they are smaller than the point size. The dotted lines are to guide the eye. The full red line is calculated from the energy-dependent local potential for ^{141}Pr-α (see Sec. II C).

C. Energy dependence of the potential

Here I discuss the extraction of a local energy-dependent potential for ^{141}Pr-α. An estimate of the uncertainties for the resulting total reaction cross section $\sigma_{\rm reac}$ will be given later in Sec. III B.

The energy dependence of the real part is weak. The volume integrals J_R in Table I increase slightly with decreasing energy; however, at even lower energies the opposite behavior is suggested from dispersion relations. Thus, the real part of the potential is simply taken from the lowest angular distribution at 19 MeV where the width parameter w is close to 1.0 and close to the average of the other energies. Note that the parameters of the real part vary only weakly with energy. This holds also for the potential derived from the analysis of the weak α-decay branch of ^{145}Pm (see Sec. II D).

The situation for the imaginary part is more difficult because the parameters vary with energy, and different parametrizations had to be used for the five angular distributions under study. For the extrapolation to low energies I use a surface Woods-Saxon potential (parameters "low energies" in Table I) with the average geometry from the angular distributions at 19.0, 23.97, and 32.0 MeV, i.e., $R_S = 1.353$ fm and $a_S = 0.530$ fm. Only the three lowest energies are considered here because these three angular distributions could be described with the same parametrization (surface Woods-Saxon) of the imaginary part. Note that the radius parameters R_S

and the diffuseness parameters a_S do not vary significantly with energy; i.e., the shape of the imaginary potential is well defined from the experimental angular distributions. (A significant energy dependence of the shape of the imaginary part is found only for halolike projectiles such as ^{6}He; see, e.g., [33].)

The strength W_S of the imaginary potential is derived by fitting the imaginary volume integral J_I of the three lowest energies using a Fermi-type function (similar to [1] and [8])

$$J_I = \frac{J_{I,0}}{1 + \exp\left[(E_0 - E_{\rm c.m.}/a_E)\right]}, \tag{4}$$

with the parameters $J_{I,0} = 74.16$ MeV fm^3, $E_0 = 17.41$ MeV, and $a_E = 2.42$ MeV; a formula similar to Eq. (4) holds for the depth W_S of the surface imaginary potential with $W_{S,0} = 31.1$ MeV. A similar Fermi-type function was also used in [8] for the depth of the imaginary volume Woods-Saxon potential. It is interesting to note that the parameters E_0 and a_E in Eq. (4) are close to the values obtained from the adjustment to the new ^{141}Pr$(\alpha,n)^{144}$Pm data in [8].

The widely used Brown-Rho parametrization of the imaginary part [35] is given by

$$J_I = J_{I,0} \frac{(E_{\rm c.m.} - E_0)^2}{(E_{\rm c.m.} - E_0)^2 + \Delta^2} \tag{5}$$

for energies $E_{\rm c.m.} > E_0$ above the opening of the first nonelastic channel at energy E_0 and $J_I = 0$ below E_0. $J_{I,0}$ is again the saturation value, and the parameter Δ describes the slope of J_I from zero to its saturation value $J_{I,0}$. E_0 is given by the excitation energy of the lowest excited state in ^{141}Pr which can be populated by inelastic scattering: $E_0 = 0.145$ MeV [36,37]. The Brown-Rho parametrization in Eq. (5) is not able to reproduce the energy dependence of the imaginary volume integrals and thus cannot be used for the extrapolation of the potential to lower energies. This may—at least partly—explain the problems with the prediction of the ^{144}Sm$(\alpha,\gamma)^{148}$Gd cross section [1] using the potential derived from ^{144}Sm$(\alpha,\alpha)^{144}$Sm elastic scattering [38] in combination with a Brown-Rho parametrization of the imaginary volume integral.

The failure of the Brown-Rho parametrization is shown in Fig. 3. Whereas the three parameters of the Fermi-type function allow a perfect reproduction of the J_I values from elastic scattering, it is impossible to reproduce the steep rise of the J_I data between about 15 and 25 MeV with a Brown-Rho function and fixed $E_0 = 0.145$ MeV. If the energy E_0 of the opening of the first nonelastic channel is taken as an additional free parameter, the J_I values from elastic scattering can be reproduced with $J_I = 76.2$ MeV fm^3, $E_0 = 15.1$ MeV, and $\Delta = 2.8$ MeV. However, this result corresponds to a vanishing imaginary part already in the energy range of the recent ^{141}Pr$(\alpha,n)^{144}$Pm experiment [8] and thus predicts that the total reaction cross section vanishes. It is clear that the Brown-Rho parametrization of the imaginary volume integral J_I cannot be used for the prediction of α-induced reaction cross sections of ^{141}Pr.
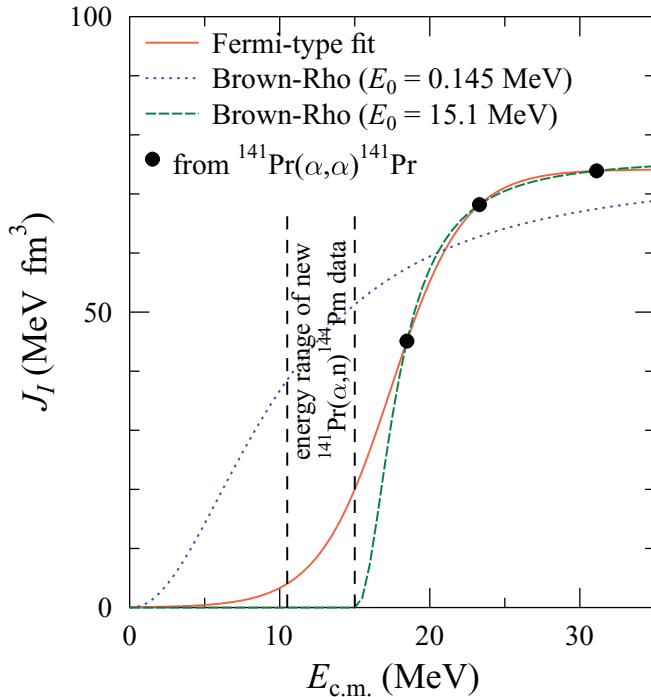
FIG. 3. (Color online) Energy dependence of the imaginary volume integral J_I using the Fermi-type parametrization of Eq. (4) (full red line) and Brown-Rho parametrizations of Eq. (5) with fixed $E_0 = 0.145$ MeV (dotted blue line) and $E_0 = 15.1$ MeV (dashed green line) with E_0 adjusted to the scattering data. The energy range of the recent ^{141}Pr(α,n)^{144}Pm experiment [8] is indicated by vertical lines. For further discussion see the text.

D. α decay of ^{145}Pm

α decay provides a further opportunity to test α-nucleus potentials at low energies. For ^{145}Pm (as in most other cases) α decay is dominated by the $\Delta L = 0$ transition from the ^{145}Pm ground state to the ^{141}Pr ground state; thus, analysis of α-decay properties provides information on the potential for the $L = 0$ partial wave (see also Sec. IV for the energy-dependent relevance of different partial waves for σ_{reac}). The mass range around $A \approx 150$ has been studied in [39] using the same type of folding potentials as in this work. Although the α-decay half-lives vary over many orders of magnitude among ^{148}Gd, ^{146}Sm, and ^{144}Nd (with their $N = 82$ daughters ^{144}Sm, ^{142}Nd, and ^{140}Ce), it has been found in [39] that the preformation of the α particle in the decaying nucleus is between about 10% and 20% within this model.

^{145}Pm with its $N = 82$ daughter ^{141}Pr has a weak α-decay branch of $(2.8 \pm 0.6) \times 10^{-9}$ [36,40,41], which, together with the half-life of $T_{1/2} = 17.7 \pm 0.4$ yr [36,40,42], translates to a partial α-decay half-life $T_{1/2}^{\alpha} = (2.0 \pm 0.4) \times 10^{17}$ s. The α-decay Q value is $Q_\alpha = 2322.2 \pm 2.6$ keV [36]. To repeat the α-decay calculations of [39] for ^{145}Pm, a real folding potential has been calculated at extremely low energies (labeled "α decay" in Table I), and the α-decay half-life has been calculated using the semiclassical model of [43]. From the ratio between the calculated half-life $T_{1/2}^{\alpha,\text{calc}} = 2.49 \times 10^{16}$ s and the experimental partial half-life a preformation

of $P = 12.5\% \pm 2.7\%$ is determined; this is within the range of 10%–20% for the neighboring α emitters with $N = 82$ daughters. Although based on almost 50-year-old data for the half-life [42] and the α branching [41], this result nicely confirms the close relationship among the various $N = 82$ nuclei including ^{144}Sm.

III. α-INDUCED REACTIONS ON ^{141}PR

As the optical potential for ^{141}Pr-α is completely fixed from the above procedure in Sec. II C, the calculation of the total reaction cross section σ_{reac} is straightforward and does not require any further parameter adjustment to experimental reaction data. First, the obtained $\sigma_{\text{reac}}(E)$ is converted to the reduced cross section σ_{red} and compared to the σ_{red} data for various projectiles and targets (full line in Fig. 2). It is obvious that the general behavior of the σ_{red} versus E_{red} energy dependence is very nicely reproduced at least down to $E_{\text{red}} \approx 0.8$ MeV, corresponding to $E_{\text{c.m.}} \approx 14$ MeV for the ^{141}Pr-α system under study in the work.

Next, the result for σ_{reac} is shown in Fig. 4 in a wide energy range, and it is converted to the astrophysical S factor in Fig. 5 for comparison with the new ^{141}Pr(α,n)^{144}Pm data of [8] for energies between 10 and 15 MeV. The new experimental S-factor data decrease with energy by about a factor of 5 from $S(E) \approx 3 \times 10^{26}$ MeV b below 11 MeV to $S(E) \approx 0.6 \times 10^{26}$ MeV b at 14.5 MeV. An excellent reproduction of the new data of [8] is found.

A. Total reaction cross section σ_{red} and cross section of the ^{141}Pr(α,n)^{144}Pm reaction

The total reaction cross section σ_{reac} is given by the sum over all nonelastic channels; i.e., it includes inelastic scattering, fusion, and all transfer channels. This σ_{reac} has to be distributed among the open channels (thresholds indicated in Fig. 4) using, e.g., the statistical model. For the particular case of the ^{141}Pr(α,n)^{144}Pm reaction in the energy range of the recent experiment [8] as shown in Fig. 5, it is found that σ_{reac} is almost identical to the (α,n) cross section because of the dominating neutron emission channel [except very close above the (α,n) threshold at 10.2 MeV]. The proton emission from the compound nucleus ^{145}Pm is strongly suppressed by the Coulomb barrier, and the ratio of (α,n) over (α,γ) cross sections is large in this energy window. Using the standard NON-SMOKER parameters [44] (α potential from [9], nucleon potentials from [45], γ-ray strength function from [46], and level density from [47]) the ratio is ≈ 4 at the lowest energy of [8] and exceeds 20 at 11.5 MeV; i.e., by neglecting the weak other open channels such as ($\alpha, \alpha n$), the total reaction cross section σ_{reac} has to be reduced by less than 5% to obtain the (α,n) cross section above 11.5 MeV and by $\approx 25\%$ for the two lowest data points. The standard TALYS [48] calculation (α potential from [49], nucleon potentials from [50], γ-ray strength function from [51], and level density from [48,52]) predicts a ratio of ≈ 10 between (α,n) and (α,γ) at the lowest energy of [8] and more than 100 at energies above ≈ 12 MeV; i.e., the (α,n) cross section does not deviate by more than 1% from σ_{reac} above 12 MeV, and the deviations at the lowest
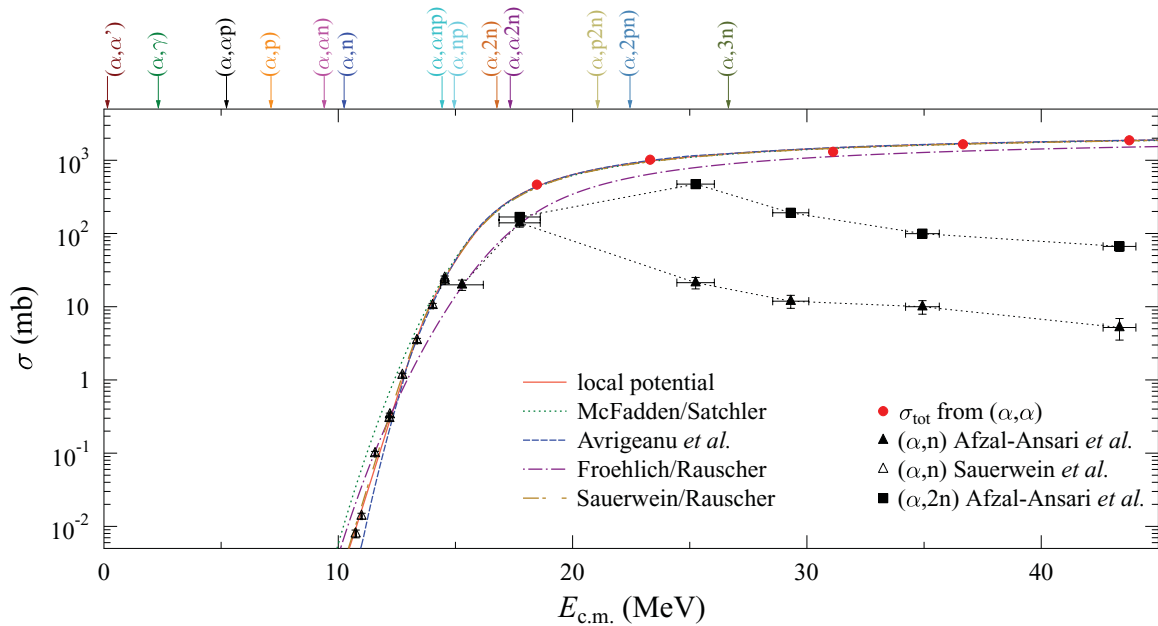
FIG. 4. (Color online) Total reaction cross sections σ_{reac} for α-induced reactions on ^{141}Pr from elastic scattering (red dots) and cross sections of the ^{141}Pr$(\alpha, n)^{144}$Pm (open and full triangles [8,18]) and ^{141}Pr$(\alpha, 2n)^{143}$Pm (full squares [18]) reactions. The data of [18] are connected by thin lines to guide the eye. Calculations with different potentials [8–11] agree well at higher energies (except [11]), but they disagree at lower energies (see also Fig. 5). The arrows on top indicate the thresholds for various reaction channels.

energies of [8] never exceed 10%. Thus, because only minor differences are predicted between the (α, n) cross section and σ_{reac} in the energy range of [8] in all calculations [44,48], I restrict myself to the presentation of σ_{reac} in Figs. 4 and 5. This avoids any uncertainties from other sources (mainly from the neutron potential and the γ-ray strength function) which may be present at the lowest data points of [8]. The minor differences between the ^{141}Pr$(\alpha, n)^{144}$Pm cross section and σ_{reac} can be seen from a comparison of the calculations in Fig. 5 of this work and Figs. 8 and 9 of [8]. (The same scale has been chosen in all these figures for simple comparison.)

From Fig. 4 it can be read that σ_{reac} is well reproduced from all potentials under study at higher energies above 25 MeV (except the FRR potential, which underestimates σ_{reac} at all energies). Discrepancies become visible at lower energies; see Fig. 5. The MCF potential shows an incorrect energy dependence and strongly overestimates the data at lowest energies. The AVR potential reproduces the experimental data in the higher energy range, but it underestimates the data at lower energies. The energy dependence calculated from the FRR potential is also incorrect, and data at low (high) energies are overestimated (underestimated). An energy-dependent potential was found in [8] which is able to reproduce the new ^{141}Pr$(\alpha, n)^{144}$Pm data over the whole measured energy range. The prediction of the new energy-dependent potential from the present study, which was adjusted only to elastic scattering data, is very close to the result of [8], but it does not require any adjustment to reaction data.

It is interesting to note that the energy of the lowest data point in Fig. 5 corresponds to a reduced energy $E_{\text{red}} \approx 0.62$ MeV which is close to the lower end of Fig. 2. The reduced cross sections σ_{red} at reduced energies below $E_{\text{red}} = 1$ MeV

are thus almost identical for ^{141}Pr $+ \alpha$ and ^{16}O $+ ^{138}$Ba; in both cases the projectile is a doubly-magic nucleus and the target is semimagic with $N = 82$.

B. Sensitivity of the total reaction cross section σ_{red} to variations of the parameters of the local potential

It is difficult to provide a precise error bar for the calculated total reaction cross section σ_{reac} in Figs. 4 and 5, but an estimate of the uncertainties can be given by reasonable variations of the parameters of the local potential, which are the geometry (in particular of the imaginary part) and the energy dependence. The results of the following sensitivity study are shown in Fig. 6. The local potential calculation (full red line, identical to Fig. 5) is the reference for the sensitivity study.

The real part of the potential is nicely constrained from the folding calculation. In addition to the scattering data, further information on the real part of the potential at very low energies can be extracted from the analysis of the α decay of ^{145}Pm (see Sec. II D). The parameters of the potential for the α-decay calculations remain close to the real part of the scattering potential. The volume integral J_R is about 10% lower than the value found for the 19-MeV scattering data. If this lower real part of the potential is used for the calculations of σ_{reac} instead of the 19-MeV real part (as derived in Sec. II C), σ_{reac} shows a slightly different energy dependence but does not change by more than about 40% in the energy range under study (dashed fuchsia line in Fig. 6). Only at very low energies below 10 MeV (i.e., below the shown energy range of Fig. 6) does the lower real potential with its resulting higher effective Coulomb barrier result in a lower σ_{reac}. But in any case the deviations remain below 50%, thus confirming that the real
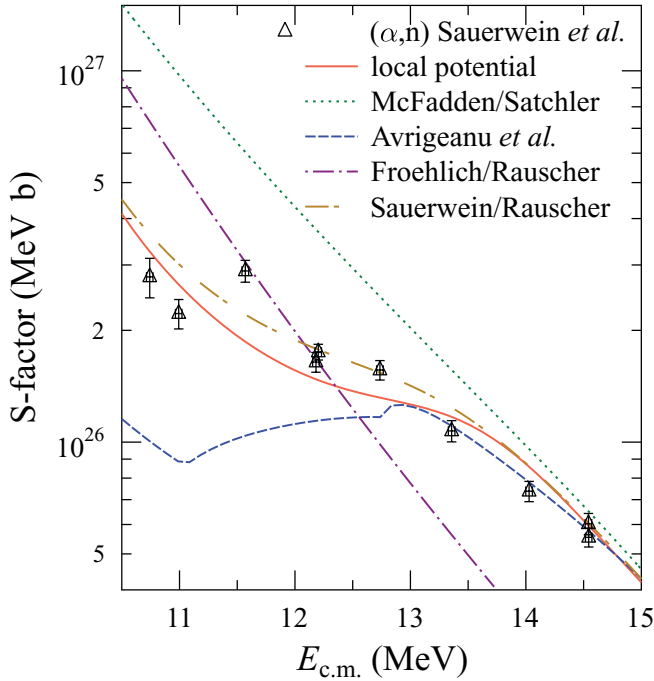
FIG. 5. (Color online) Same as Fig. 4, but shown as astrophysical S factor in a narrow energy window around the new experimental data of [8]. For simplicity, the averaged S factor at the mean energy (see Table III of [8]) is shown here. The local potential (full red line) and the SAR potential (dash-dotted golden) reproduce the data well, but the global potentials fail to reproduce the energy dependence (MCF: dotted green; AVR: dashed blue; FRR: dash-dotted dark-magenta).
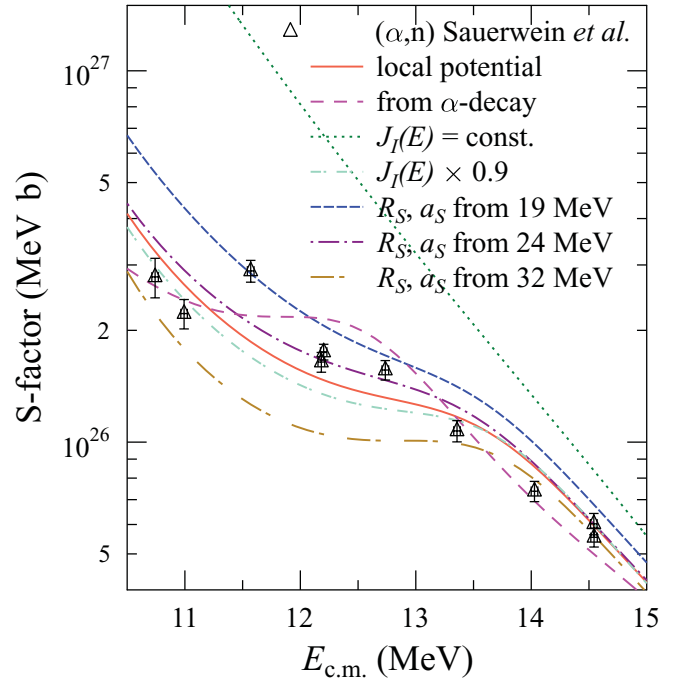
FIG. 6. (Color online) Sensitivity of the astrophysical S factor to variations of the potential parameters. The full red line is identical to the previous Fig. 5. A reduced real potential (derived from α decay; see Sec. II D) shows a slightly different energy dependence (dashed magenta). Neglecting the energy dependence of the imaginary part leads to strong overestimation of the experimental cross sections (green dotted), whereas small modifications of the imaginary part (10% reduction of the strength or variation of geometry parameters) do not affect the calculated $\sigma_{\rm reac}$ strongly. For further discussion see the text.

part of the potential is relatively well defined and does not lead to big uncertainties in the calculation of $\sigma_{\rm reac}$ in the energy range under analysis.

It should be noted that the α-decay potential is adjusted at the decay energy of 2.3 MeV, far below the energy range under study; thus, using the α-decay potential for the calculation of $\sigma_{\rm reac}$ is an extremely careful estimate for the uncertainty of $\sigma_{\rm reac}$ on a variation of the real potential. I do not show calculations with increased strength of the real part because volume integrals significantly above 350 MeV fm^3 have not been observed in α scattering of semimagic nuclei [15,16,19,53]. This finding is supported theoretically by the fact that dispersion relations lead to a reduction of real potential at very low energies (see, e.g., Fig. 11 of [15] or Fig. 12 of [54]).

The influence of the imaginary part on the calculated total reaction cross section $\sigma_{\rm reac}$ is significant. In particular, a reasonable energy dependence is essential for the reproduction of the experimental data. If the energy dependence of the imaginary part is ignored and the saturation value $J_{I,0}$ is used instead of the energy dependence of Eq. (4), then $\sigma_{\rm reac}$ is overestimated with increasing discrepancy to the experimental data at lower energies (green dotted line in Fig. 6). A similar behavior has been found for the energy-independent MCF potential. However, small variations of the imaginary strength result only in minor modifications of $\sigma_{\rm reac}$: a reduction of $J_I(E)$ by 10% leads to slightly reduced $\sigma_{\rm reac}$ with very similar energy dependence as the reference calculation (dash-dotted aquamarine line).

Next, the geometry parameters of the surface Woods-Saxon potential in the imaginary part were taken from the three angular distributions at 19, 24, and 32 MeV (see Table I) instead of their average values $R_S = 1.353$ fm and $a_S = 0.530$ fm. The depth W_S has been adjusted to the same volume integral in Eq. (4) as in the reference calculation. The geometry from the 19-MeV angular distribution leads to somewhat larger $\sigma_{\rm reac}$, which is a consequence of the larger $a_S = 0.581$ fm (short-dashed blue). The result from the 24-MeV geometry is almost identical to the reference calculation (dash-dotted magenta line), and the result from the 32-MeV geometry is somewhat smaller than the reference (dash-dotted golden line). The uncertainty of the geometry of the imaginary potential leads to uncertainties of $\sigma_{\rm reac}$ of the order of 30%. It has to be pointed out that such a small uncertainty can only be achieved because the geometry parameters are well defined from several angular distributions at energies around and slightly above the Coulomb barrier.

Summarizing the above sensitivity study, we have found that the uncertainty of $\sigma_{\rm reac}$ from the present local potential is much smaller than the variations among the different predictions from global potentials. The influence of the geometry of the imaginary part is not dramatic as long as the geometry is well defined from low-energy scattering data. However, the energy dependence of the strength J_I of the

imaginary part is an essential ingredient for the prediction of reaction cross sections below the Coulomb barrier.

IV. DISCUSSION

Let me start the discussion with a few general remarks on statistical model calculations. In the statistical model the cross section for a reaction is given by the product of the compound formation cross section and the decay branching of the decaying compound nucleus into the particular channel. The full formalism can be found, e.g., in [21,44]. The formation cross section is calculated from transmission coefficients using the optical potentials; i.e. it is the total reaction cross section $\sigma_{\rm reac}$ in Eq. (1). The decay branching is also calculated from transmission coefficients for particle channels and from the γ-ray strength function for the photon (capture) channel. It is obvious that the correct reproduction of the total reaction cross section $\sigma_{\rm reac}$ is the basic prerequisite for a successful prediction of any reaction cross section in the statistical model and should thus always be discussed first in presentations of statistical model calculations. Unfortunately, this is not always the case.

The total reaction cross section $\sigma_{\rm reac}$ is then distributed among all open channels. It is important to study the influence of all open channels and their relevance for the decay branching of the compound nucleus. This is nicely illustrated in Fig. 4. Close above the opening of the $(\alpha,2n)$ channel around 17 MeV, the $(\alpha,2n)$ channel becomes stronger than the (α,n) channel, which was dominant from close above its threshold at 10.2 MeV up to 17 MeV. If an open channel, e.g., the $^{141}{\rm Pr}(\alpha,2n)^{143}{\rm Pm}$ channel above 17 MeV, is not taken into account in a statistical model calculation, then all the calculated $^{141}{\rm Pr}(\alpha,X)$ cross sections above 17 MeV must be overestimated. However, such a shortcoming of neglected open channels may be partly compensated by using special potentials for the particular (α,X) reaction under study.

After these general remarks let me be more specific for α-induced reactions on $^{141}{\rm Pr}$. The total reaction cross section $\sigma_{\rm reac}$ is well understood and has relatively small uncertainties for energies above the Coulomb barrier. This can be seen from the comparison of predicted $\sigma_{\rm reac}$ from the various global potentials [9–11] to the experimental result from the analysis of the elastic scattering angular distributions (see Table II). All potentials (except the FRR potential) reproduce the experimental $\sigma_{\rm reac}$ within minor uncertainties of typically a few percent.

The excellent reproduction of $\sigma_{\rm reac}$ for most global potentials at energies above the Coulomb barrier can be explained by a look at the reflection coefficients η_L and the contribution σ_L of the Lth partial wave to $\sigma_{\rm reac}$ (see Fig. 7 for the example of the $E_{\rm c.m.} = 23.31$ MeV data). For small angular momenta L the reflection coefficients are close to $\eta_L \approx 0$; thus, σ_L increases linearly proportional to $2L + 1$ (dashed line in Fig. 7). All global potentials with a reasonable real part and a sufficiently strong imaginary part, i.e., the MCF, AVR, and SAR potentials, predict the same σ_L for small L. For large L (corresponding to large impact parameters) the η_L values approach unity, and the σ_L vanish (i.e., partial waves with large angular momenta

TABLE II. Experimental total reaction cross sections $\sigma_{\rm reac}$ (in millibarns) derived from $^{141}{\rm Pr}(\alpha,\alpha)^{141}{\rm Pr}$ elastic scattering angular distributions (from Table I), compared to the phase-shift analysis ("PSA"), predictions from the global α-nucleus potentials MCF, AVR, and FRR [9–11], and the energy-dependent potential SAR of [8] which was adjusted to reproduce the $^{141}{\rm Pr}(\alpha,n)^{144}{\rm Pm}$ cross section at low energies.

$E_{\rm c.m.}$ (MeV)	Exp.	PSA	MCF	AVR	FRR	SAR
18.48	465 ± 31	433	425	437	197	424
23.31	1018 ± 31	1003	957	993	648	957
31.12	1306 ± 39	1310	1452	1487	1125	1452
36.66	1654 ± 50	1654	1662	1696	1333	1662
43.76	1874 ± 56	1873	1841	1872	1514	1841

are practically not absorbed by any imaginary potential with a limited radial range). Differences in σ_L appear only for a few partial waves between $L \approx 8$ and $L \approx 14$ (for the $E_{\rm c.m.} = 23.31$ MeV case) where the different potentials predict different η_L and thus different σ_L. It becomes obvious that relatively small differences in η_L for a very limited number of partial waves around $L \approx 10$ cannot lead to major differences for the total reaction cross section $\sigma_{\rm reac}$, which is simply given by the sum over all σ_L. The good reproduction of the total reaction cross section $\sigma_{\rm reac}$ from different global potentials is thus simply a consequence of intrinsic properties of the scattering matrix as long as the energy exceeds the Coulomb barrier.

The situation changes dramatically at lower energies far below the Coulomb barrier. Here only the lowest angular momenta (below $L \approx 5$) are affected, show $\eta_L < 1$, and thus contribute to σ_L; but even these η_L remain much larger than zero and do even approach $\eta_L \approx 1$ for very low energies (see Fig. 8 for energies $11 \leqslant E_{\rm c.m.} \leqslant 15$ MeV, i.e., the energy range of the new $^{141}{\rm Pr}(\alpha,n)^{144}{\rm Pm}$ data of [8]). Here the trivial $2L + 1$ proportionality of σ_L vanishes. Now the relevant σ_L
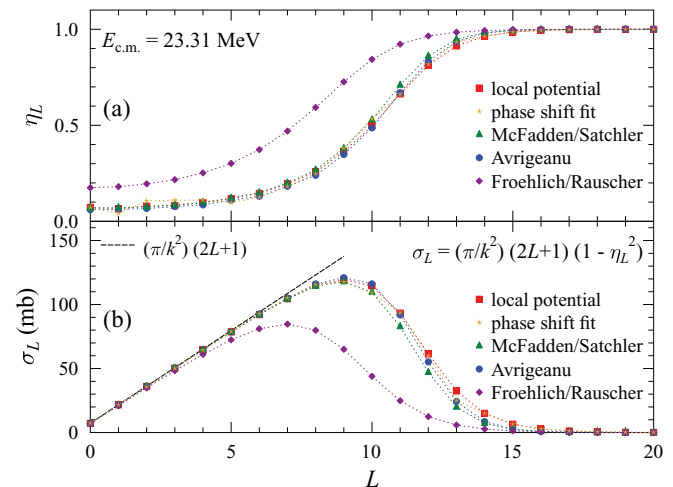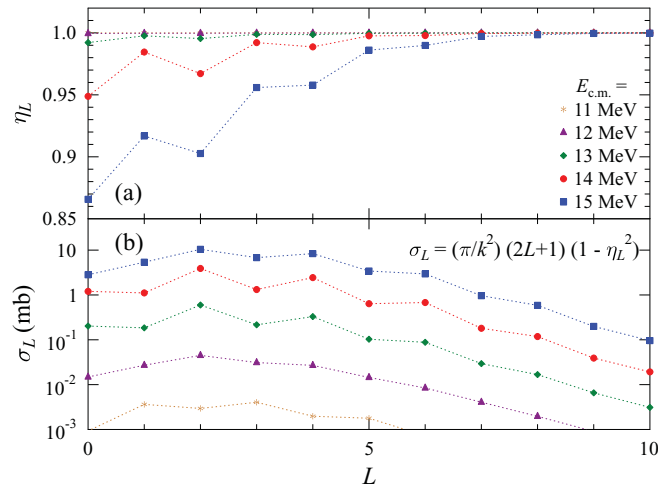

FIG. 7. (Color online) Reflection coefficients η_L (a) and contribution σ_L of the Lth partial wave to the total reaction cross section $\sigma_{\rm reac}$ (b); linear scale]. The thin dotted lines connect the data points to guide the eye. For further discussion see the text.

FIG. 8. (Color online) Reflection coefficients η_L (a) and contribution σ_L of the Lth partial wave to the total reaction cross section σ_{reac} [(b); logarithmic scale] for low energies between 11 and 15 MeV. Note the different scale for η_L in Figs. 7 and 8. The thin dotted lines connect the data points to guide the eye. The η_L values at 11 and 12 MeV are very close to unity for all L; thus, the 11-MeV data disappear behind the 12-MeV data in the upper diagram. Differences between the 11- and 12-MeV data become visible only in the presentation of σ_L, which is proportional to $(1 - \eta_L^2)$. The $2L + 1$ proportionality of σ_L for small L (as seen at higher energies in Fig. 7) vanishes completely at energies below the Coulomb barrier. For further discussion see the text.

depend sensitively on details of the potential. In particular, the strength of the imaginary part for large radii has strong impact on the resulting cross sections σ_L. Under these conditions it becomes mandatory that the imaginary potential has the proper geometry (e.g., fixed from scattering data at slightly higher energies) and the proper strength (using a realistic energy dependence, e.g., from Eq. (4), which can be adjusted to scattering data and/or properly chosen reaction data). As pointed out in Sec. II, the real part of the potential has only minor uncertainties in shape and strength because it is calculated from a folding procedure; furthermore, the analysis of α-decay properties provides a test for the $L = 0$ potential (see Sec. II D).

The above discussion explains why all global potentials are able to reproduce total reaction cross sections σ_{reac} above the Coulomb barrier but may fail to reproduce σ_{reac} below the Coulomb barrier. Thus, it is not surprising that the global potentials show a significant scatter in the predictions of the new experimental ^{141}Pr(α,n)^{144}Pm data of [8] (see Fig. 5).

For the energy-independent MCF potential the reason for the discrepancy is obvious. The missing energy dependence of the MCF potential leads to an overestimation of the imaginary part of the potential at low energies and thus to an overestimation of the ^{141}Pr(α,n)^{144}Pm cross section. As expected, the discrepancy between the MCF prediction and the experimental data increases with decreasing energy. A similar behavior has been found in other cases; see, e.g., the ^{144}Sm(α,γ)^{148}Gd reaction [1], the ^{112}Sn(α,γ)^{116}Te reaction [3], or the ^{106}Cd(α,γ)^{110}Sn reaction [2].

It is difficult to make such general statements on the many-parameter AVR potential. This potential has been adjusted to a huge data base of elastic scattering and reaction data [55], and excellent agreement has been found for many reactions especially in the $A \approx 100$ range. The AVR potential shows the best agreement of the global potentials with the elastic scattering angular distributions, and it reproduces the ^{141}Pr(α, n)^{144}Pm data well at higher energies above 13 MeV. However, it underestimates the data at lower energies significantly.

The FRR potential has been optimized for reaction data at low energies. Its parameters are energy-independent and close to the MCF potential in most cases. Similar to the MCF case, because of its energy independence it cannot be expected that the FRR potential is able to reproduce simultaneously elastic scattering data above the Coulomb barrier and reaction data below the Coulomb barrier. Despite the big success in predicting reaction cross sections at low energies, the simple FRR potential cannot be the basis for a global potential in a broad energy range.

The MCF potential with an additional energy dependence of the depth of the imaginary potential has been used in [8] to reproduce their new ^{141}Pr(α,n)^{144}Pm data. Although this is in principle the best way to improve the MCF potential, there are two disadvantages of the SAR potential. Obviously, reaction data are required to fit the energy dependence of the SAR potential. And, in addition, the chosen underlying MCF potential uses a volume Woods-Saxon imaginary part which has been found—according to recent studies [17,19,20]—to be probably not fully adequate for low energies below the Coulomb barrier; here surface Woods-Saxon potentials should be preferred. Consequently, the SAR potential is not able to reproduce the elastic scattering angular distributions. It turns out that the angular distributions of the SAR and MCF potentials are almost identical above 25 MeV because the MCF and SAR potentials are almost identical there. Even at 19 MeV where the imaginary depth of the SAR potential is about 25% lower than the MCF depth, the calculated angular distributions of MCF and SAR agree within a few percent, i.e., within a linewidth in Fig. 1; therefore, the SAR potential is not shown in Fig. 1.

The energy-dependent potential of this work has been derived from elastic scattering data. Local optical potentials have been derived from the available angular distributions between 19 and 45 MeV by fitting the parameters of the real part (strength and width of the folding potential) and the imaginary part (Woods-Saxon parametrization). Because of the small variation of the found parameters at the different energies (see Table I), these parameters could be combined to derive a common potential with an energy-dependent depth of the imaginary surface potential. This common potential maintains the good reproduction of the elastic scattering data and the derived total reaction cross sections σ_{reac}. In addition, it turns out that this potential is able to predict the cross section of the ^{141}Pr(α,n)^{144}Pm cross section at lower energies, in particular in the energy range of the new experimental data of [8] between 10 and 15 MeV (see Fig. 5). Thus, the new potential is able to describe ^{141}Pr(α,α)^{141}Pr elastic scattering data at energies around and above the Coulomb

barrier simultaneously with ^{141}Pr$(\alpha,n)^{144}$Pm reaction data below the Coulomb barrier.

The parametrization of this new potential, i.e., a double-folding potential in the real part and a surface Woods-Saxon potential with fixed geometry and energy-dependent depth, should be tested in further cases in forthcoming work. For a detailed study of a particular target nucleus, several elastic scattering angular distributions are required to fix the shape and the energy dependence of the imaginary potential. However, the found geometry parameters in the present ^{141}Pr-α case ($R_S = 1.353$ fm and $a_S = 0.530$ fm) are close to standard values; it should be possible to apply these parameters to other target nuclei. The main problem will be the determination of the energy dependence of the depth of the imaginary surface potential. Here considerations similar to [8,10,55] will be helpful where parameters of the imaginary part have been put in relation to the Coulomb barrier. It is obvious that the predictions from such a potential have to be compared to experimental reaction data below the Coulomb barrier, which are—despite significant improvement in the recent years—still not widely available.

The previous discussion may also be summarized to provide a general recipe to find a widely useful potential. First, the potential has to reproduce the total reaction cross section σ_{reac} at energies above the Coulomb barrier. However, because of the $2L + 1$ proportionality of σ_L for small L, this requirement is almost trivial and can be fulfilled by many potentials. Next, among the many α-nucleus potentials which are able to fulfill this first condition, these potentials have to be selected which are in addition able to reproduce the elastic scattering angular distributions. This ensures the correct strength and geometry of the chosen potential (in particular of the imaginary part), which is essential for the prediction of σ_{reac} below the Coulomb barrier. This conclusion is also a strong motivation to extend the measurements of elastic scattering angular distributions.

V. SUMMARY AND CONCLUSIONS

A new local potential for the system ^{141}Pr-α has been derived from elastic scattering angular distributions. The derived potential is able to predict the total reaction cross section σ_{reac} which is dominated by the ^{141}Pr$(\alpha,n)^{144}$Pm cross section in the energy range of the new experimental data of [8]. Thus, the new potential for ^{141}Pr-α is able for the first time to describe simultaneously elastic scattering data around

and above the Coulomb barrier and reaction data below the Coulomb barrier. Such a simultaneous description was not achieved and/or aimed for in earlier work using the global potentials of [9–11] or the local potential suggested in [8].

Reasons for the partial success at higher energies and failure at lower energies of global potentials are carefully analyzed by studying the reflection coefficients η_L and the contribution σ_L of the Lth partial wave to the total reaction cross section σ_{reac}. It is found that above the Coulomb barrier σ_L for small angular momenta are predicted correctly by most global potentials because of a simple $2L + 1$ proportionality, which is almost independent of details of the optical potential. This results in minor differences for the total reaction cross section σ_{reac}, which have to arise from a few partial waves around $L \approx 10$ for the ^{141}Pr-α case under study in this work. However, at low energies below the Coulomb barrier this simple $2L + 1$ proportionality of σ_L for small L vanishes, the σ_L values become sensitive to details of the potential, and consequently predictions for σ_{reac} from global potentials show a huge spread. Precise scattering data at different energies around and closely above the Coulomb barrier are required to determine a potential (in particular the shape and strength of its imaginary part) which is able to predict total reaction cross sections σ_{reac} not only above but also below the Coulomb barrier.

Because the new local potential has a well-defined geometry derived from elastic scattering, its extrapolation to low energies and its predictions for σ_L and the resulting σ_{reac} should be more reliable than predictions from other global potentials. The parametrization of the new local potential may finally become the basis for a new global potential to solve or at least reduce the long-standing problem of α-nucleus potentials at low energies below the Coulomb barrier and the resulting uncertainties for the prediction of α-induced reaction cross sections at astrophysically relevant energies.

[1] E. Somorjai *et al.*, Astron. Astrophys. **333**, 1112 (1998).
[2] Gy. Gyürky *et al.*, Phys. Rev. C **74**, 025805 (2006).
[3] N. Özkan *et al.*, Phys. Rev. C **75**, 025801 (2007).
[4] I. Cata-Danil *et al.*, Phys. Rev. C **78**, 035803 (2008).
[5] C. Yalcin *et al.*, Phys. Rev. C **79**, 065801 (2009).
[6] Gy. Gyürky *et al.*, J. Phys. G **37**, 115201 (2010).
[7] G. G. Kiss *et al.*, Phys. Lett. B **695**, 419 (2011).
[8] A. Sauerwein *et al.*, Phys. Rev. C **84**, 045808 (2011).
[9] L. McFadden and G. R. Satchler, Nucl. Phys. **84**, 177 (1966).
[10] M. Avrigeanu and V. Avrigeanu, Phys. Rev. C **82**, 014606 (2010).
[11] T. Rauscher, Nucl. Phys. A **719**, C73 (2003); **725**, 295(E) (2003).
[12] EXFOR data base, [http://www-nds.iaea.org/exfor/exfor.htm], Version June 24, 2011.
[13] H. W. Baer, H. C. Griffin, and W. S. Gray, Phys. Rev. C **3**, 1398 (1971).
[14] P. Guazzoni and L. Zetta (private communication to G. Staudt, 1994).

[15] U. Atzrott, P. Mohr, H. Abele, C. Hillenmayer, and G. Staudt, Phys. Rev. C **53**, 1336 (1996).

[16] G. G. Kiss *et al.*, Phys. Rev. C **80**, 045807 (2009).

[17] G. G. Kiss *et al.*, Phys. Rev. C **83**, 065807 (2011).

[18] M. Afzal Ansari, N. P. M. Sathik, D. Singh, and M. H. Rashid, J. Phys. Soc. Jpn. **74**, 1150 (2005).

[19] D. Galaviz, Zs. Fülöp, Gy. Gyürky, Z. Máté, P. Mohr, T. Rauscher, E. Somorjai, and A. Zilges, Phys. Rev. C **71**, 065802 (2005).

[20] H. Guo, Y. Xu, H. Liang, Y. Han, and Q. Shen, Phys. Rev. C **83**, 064618 (2011).

[21] T. Rauscher, Int. J. Mod. Phys. E **20**, 1071 (2011).

[22] V. Chisté, R. Lichtenthäler, A. C. C. Villari, and L. C. Gomes, Phys. Rev. C **54**, 784 (1996).

[23] H. Abele, U. Atzrott, A. Auce, C. Hillenmayer, A. Ingemarsson, and G. Staudt, Phys. Rev. C **50**, R10 (1994).

[24] A. Auce, R. F. Carlson, A. J. Cox, A. Ingemarsson, R. Johansson, P. U. Renberg, O. Sundberg, G. Tibell, and R. Zorro, Phys. Rev. C **50**, 871 (1994).

[25] S. Ait-Tahar and Y. Nedjadi, Phys. Rev. C **52**, 415 (1995).

[26] A. Kumar, S. Kailas, S. Rathi, and K. Mahata, Nucl. Phys. A **776**, 105 (2006).

[27] P. Demetriou and M. Axiotis, AIP Conf. Proc. **891**, 281 (2007).

[28] P. Demetriou, A. Lagoyannis, A. Spyrou, H. W. Becker, T. Konstantinopoulos, M. Axiotis, and S. Harissopulos, AIP Conf. Proc. **1090**, 293 (2009).

[29] P. Demetriou, C. Grama, and S. Goriely, Nucl. Phys. A **707**, 253 (2002).

[30] A. Palumbo, W. P. Tan *et al.* (to be published).

[31] P. Mohr, D. Galaviz, Zs. Fülöp, Gy. Gyürky, G. G. Kiss, and E. Somorjai, Phys. Rev. C **82**, 047601 (2010).

[32] P. N. de Faria *et al.*, Phys. Rev. C **81**, 044605 (2010).

[33] P. Mohr *et al.*, Phys. Rev. C **82**, 044606 (2010).

[34] P. Mohr, International Workshop on the p-process: Status and Outlook, Istanbul, 2011 (to be published).

[35] G. E. Brown and M. Rho, Nucl. Phys. A **372**, 397 (1981).

[36] Online database ENSDF [http://www.nndc.bnl.gov/ensdf/].

[37] J. K. Tuli and D. F. Winchell, Nucl. Data Sheets **92**, 277 (2001).

[38] P. Mohr, T. Rauscher, H. Oberhummer, Z. Máté, Zs. Fülöp, E. Somorjai, M. Jaeger, and G. Staudt, Phys. Rev. C **55**, 1523 (1997).

[39] P. Mohr, Phys. Rev. C **61**, 045802 (2000).

[40] E. Browne and J. K. Tuli, Nucl. Data Sheets **110**, 507 (2009).

[41] M. Nurmia, P. Kauranen, and A. Siivola, Phys. Rev. **127**, 943 (1962).

[42] A. R. Brosi, B. H. Ketelle, H. C. Thomas, and R. J. Kerr, Phys. Rev. **113**, 239 (1959).

[43] S. A. Gurvitz and G. Kälbermann, Phys. Rev. Lett. **59**, 262 (1987).

[44] T. Rauscher and F.-K. Thielemann, At. Data Nucl. Data Tables **75**, 1 (2000).

[45] J. P. Jeukenne, A. Lejeune, and C. Mahaux, Phys. Rev. C **16**, 80 (1977).

[46] C. M. McCullagh, M. L. Stelts, and R. E. Chrien, Phys. Rev. C **23**, 1394 (1981).

[47] T. Rauscher, F.-K. Thielemann, and K.-L. Kratz, Phys. Rev. C **56**, 1613 (1997).

[48] A. J. Koning, S. Hilaire, and M. C. Duijvestijn, in *Proceedings of the International Conference on Nuclear Data for Science and Technology, April 22–27, 2007, Nice, France*, edited by O. Bersillon, F. Gunsing, E. Bauge, R. Jacqmin, and S. Leray (EDP Sciences, Les Ulis, France, 2008), pp. 211–214; TALYS version 1.2 from www.talys.eu.

[49] S. Watanabe, Nucl. Phys. **8**, 484 (1958).

[50] A. J. Koning and J. P. Delaroche, Nucl. Phys. A **713**, 231 (2003).

[51] J. Kopecky and M. Uhl, Phys. Rev. C **41**, 1941 (1990).

[52] T. Ericson, Adv. Phys. **9**, 425 (1960).

[53] Zs. Fülöp *et al.*, Phys. Rev. C **64**, 065805 (2001).

[54] H. Abele and G. Staudt, Phys. Rev. C **47**, 742 (1993).

[55] M. Avrigeanu, A. C. Obreja, F. L. Roman, V. Avrigeanu, and W. von Oertzen, At. Data Nucl. Data Tables **95**, 501 (2009).